Minimax Theory and its Applications
Volume 11 (2026), No. 3s, 1062 to 1073

Minimax-Based Finite Element Analysis of Electromechanical Interaction in a Piezoelectric Cantilevered Beam Using MATLAB

Ahmad Ikhwan Mohd Zubir[1], Nur Hidayah Mansor[1*]

[1] School of Mechanical Engineering, Engineering Campus Tuanku Syed Sirajuddin, Universiti Sains Malaysia, Nibong Tebal, 14300, Pulau Pinang, Malaysia
* Corresponding Author: menurhidayah@usm.my

Abstract

The dimensions and loading of piezoelectric cantilever beams influence their coupled mechanical and electrical responses. This paper investigates the effects of beam length, width, and applied tip force on static displacement and electrical potential using a hybrid finite element and moving average approach. A mathematical model describing the governing electromechanical equations was developed and solved using eight-node quadratic quadrilateral finite elements. A moving average filter was then applied to smooth the numerical results and reduce fluctuations associated with differences in scale. The model was evaluated, followed by a parametric study of beam geometry and loading. With 30,000 elements, the filtered model predicts an electrical potential of 1.1376 mV. The corresponding differences in displacement and electrical potential are approximately 3.6% and 1.3%, respectively. The parametric study considers beam lengths of 80 to140 mm, widths of 40 to 80 mm, and tip forces of 0.05 to 1.2 N. Under a tip force of 1.2 N, increasing the beam length from 80 to 140 mm at a fixed width of 40 mm increases the electrical potential from 10.19 to 45.69 mV. Increasing the width from 40 to 80 mm at a fixed length of 120 mm reduces the electrical potential from 29.85 to 5.06 mV. Both displacement and electrical potential increase approximately linearly with applied force. These findings characterise the sensitivity of the modelled cantilevers to geometry and loading under static conditions and may inform the preliminary design of piezoelectric energy harvesters intended for energy harvester device applications.

Keywords: Piezoelectric energy harvester, Piezoelectric cantilever beam, Finite element method, electromechanical analysis, moving-average post-processing

1. Introduction

Piezoelectric energy harvesting converts mechanical energy from ambient vibrations into electrical energy through the direct piezoelectric effect . Deformation of a piezoelectric material generates electrical charge, providing a potential energy source for low-power electronics [1]. This approach is relevant to wireless sensor networks, where battery replacement or recharging can constrain long-term operation [2]. Cantilever harvesters incorporating lead zirconate titanate (PZT) patches are widely investigated because bending produces strain in the active material and their structural parameters can be adjusted to suit the excitation conditions[3]. Their electrical response depends on the interaction between structural deformation, piezoelectric coupling, and electrical boundary conditions[4].

The geometry and coverage of the piezoelectric patch are central to this interaction. Changing patch length or width changes the amount of active material, electrode area, and contribution of the patch to the stiffness and mass of the composite beam. These changes also affect capacitance and the strain distribution sampled by the electrodes. Consequently, increasing patch dimensions does not necessarily produce a proportional increase in voltage or harvested power. Analytical and experimental investigations of partially covered cantilevers have examined the effects of piezoelectric coverage on harvester response [5]. Studies of varying beam cross-sections and shape optimisation further demonstrate the importance of geometry in determining electromechanical performance [6,7]. A systematic assessment of patch dimensions therefore requires a coupled formulation that resolves both displacement and electrical potential.

Fundamentally, the oscillations of a cantilever beam will produced the vibration. The resulting motion is governed by the system's mass, stiffness, and damping, which determine its natural frequencies, resistance to deformation, and rate of energy dissipation [8]. Thus this mechanism can be complex because they contain many interacting components and material properties. simplified or reduced-order models are often used to reduce computational effort while

retaining the behaviour relevant to the analysis. However, these models should preserve essential physical properties, such as stability and energy relationships, to provide reliable predictions [9]. Therefore, understanding the interaction between electromechanical coupling and mechanical properties is of great interest in determining the power output.
Several modelling approaches have been developed for piezoelectric cantilevers. For example, simplified lumped-parameter models demonstrate how mechanical and electrical loads affect system performance [10]. Additionally, models based on continuous systems theory, which include electromechanical coupling, provide more accurate predictions of energy output and dynamic behaviour [11] and help clarify how mechanical vibrations interact with electrical fields generated. The Runge-Kutta method shows that increasing tip masses and excitation amplitudes can boost voltage output [12]. Analytical models allow parametric studies to optimise resistive load and damping ratio, enhancing beam performance [13]. Researchers have used Euler-Bernoulli and Rayleigh-Ritz models for beam analysis; however, these are limited to simple geometries and conditions [14]. A theoretical framework examining the relationship between voltage and vibration in beams has also been proposed [15].
Despite these advancements, many studies tend to overlook complex material behaviours in modelling beam voltage output, necessitating robust numerical simulations [16]. Additionally, mathematical models have been employed to evaluate the influence of amplifiers on beam performance [17]. Accurate coupled electromechanical motion equations are essential for precise modelling and performance assessment [18]. To address these limitations, the finite element method (FEM) has gained prominence in PEH beam analysis, owing to its ability to handle complex geometries and coupled phenomena. FEM allows for flexible meshing and high-fidelity simulations under diverse boundary conditions [19]. Consequently, numerous studies utilise commercial finite element analysis (FEA) software for PEH applications [20–22]. These investigations show how variables such as beam dimensions, substrate stiffness, and proof mass distribution influence energy harvesting efficiency [23,24]. Furthermore, FEM analyses continue to evaluate the performance and efficiency of beams as energy harvesters [25,26]. However, optimising output power remains a challenge due to complex electromechanical interactions, nonlinearities, and environmental factors affecting system behaviour [27].

However, the existing classical linear models used in FEM analyses tend to oversimplify electromechanical coupling, leading to discrepancies between simulations and experimental results [28]. As a result, these models often face numerical instabilities, which can manifest as unphysical results, misleading oscillations, or convergence issues, requiring post-processing techniques for improvement [29]. These problems mainly arise from factors such as the high stiffness matrix ill-conditioning caused by material anisotropy and electromechanical coupling, as well as the mesh sensitivity needed to accurately capture polarisation effects and high-strain gradients [30, 31]. Addressing these numerical challenges is crucial to ensure that the simulation results accurately reflect the model's behaviour. Prior research used triangular and tetrahedral shape functions in [32] to improve the finite element analysis of piezoelectric materials. Additionally, a new hybrid FEM zig-zag theory with similar aims was introduced in [33]. These approaches address the representation of coupled fields and structural deformation within the numerical formulation. Post-processing of a computed response serves a different purpose: smoothing may assist interpretation, but it cannot by itself establish convergence or correct an inaccurate governing model. Any assessment of a smoothing procedure should therefore distinguish changes in the displayed response from changes in the underlying finite element solution.
When tackling the computations involved in finite element method (FEM) analysis, MATLAB stands out as an exceptional tool compared to other software options. MATLAB provides a practical environment for implementing coupled finite element equations because element assembly, numerical integration, and solution procedures can be expressed directly using matrix operations. A custom implementation also permits controlled changes to patch geometry and consistent extraction of displacement and electrical potential across successive analyses. Although previous studies have investigated patch coverage and harvester geometry [34], the present work focuses specifically on the influence of patch length and width on the static electromechanical response of a cantilever beam. This paper implemented a MATLAB finite element model to evaluate cantilever displacement and electrical potential for different piezoelectric patch lengths and widths under prescribed mechanical loading. Furthermore, a moving average (MA) post-processing technique is applied to evaluates static deformation and electrical power under base excitation. This approach allows for the modelling and analysis of the harvester's behaviour, focusing on determining the displacement and electrical potential through static analysis. Additionally, the study examines how the harvester's performance is affected by several features, including beam length, width, and applied force.

2. Piezoelectric Cantilever Beam Design Modelling

Figure 1 shows the 120 mm length, 40 mm width, and 1 mm thickness of the PCB beam design model. The piezoelectric energy-harvesting beam is a unimorph cantilever comprising a single lead zirconate titanate Type 5H (PZT-5H) layer bonded to an aluminium alloy substrate. PZT-5H was selected for its high piezoelectric coefficients, while the aluminium alloy substrate provides structural support. One end of the composite beam is clamped, and the

opposite end remains free to deform under the applied loading. The dimensions of the piezoelectric and substrate beam are listed in Table 3.1.

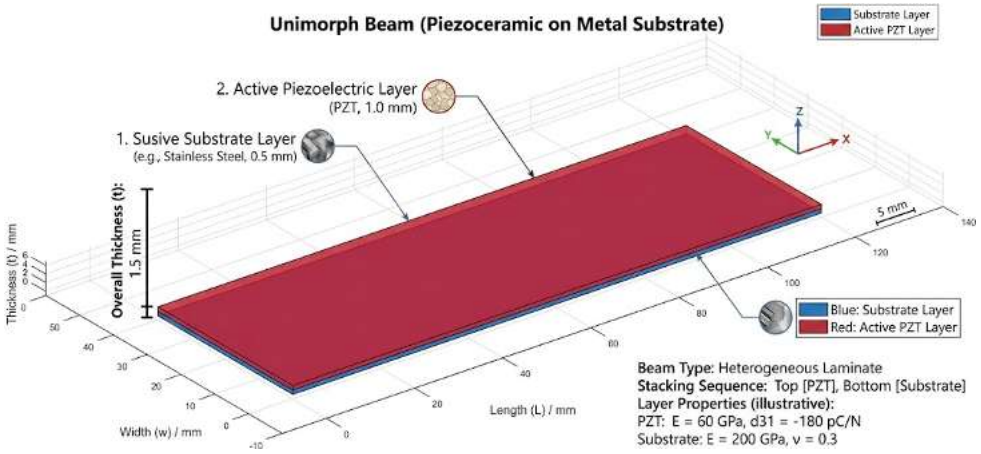


Figure 1. Unimorph cantilever beam design model.

Table 1. Dimension for piezoelectric and substrate layer beams

Length of piezoelectric beam, mm	120
Length of substrate layer, mm	120
Width of piezoelectric beam, mm	40
Width of substrate layer, mm	40
Thickness of piezoelectric beam, mm	1
Thickness of substrate layer, mm	1
External force, N	0.05

3. Finite Element Method Implementation in MATLAB

A coupled electromechanical finite element procedure was implemented in MATLAB to calculate the static displacement and open-circuit voltage of a PZT-5H/aluminium unimorph cantilever. The formulation assumes small deformation, linear elastic and piezoelectric behaviour, and perfect bonding between the piezoelectric and aluminium layers. Inertia and damping are excluded from the static solution. The two-dimensional computational domain was discretized using eight-node quadratic serendipity quadrilateral elements. For a rectangular domain with dimensions L_x and L_y, the nominal element dimensions are

$$h_x = \frac{L_x}{n_{\mathrm{el},x}}, \qquad h_y = \frac{L_y}{n_{\mathrm{el},y}}. \qquad (1)$$

Here, $n_{\mathrm{el},x}$ and $n_{\mathrm{el},y}$ denote the numbers of elements along the two model coordinates. Each element contains four corner nodes and four midside nodes. The element connectivity follows the local ordering used in the shape functions, and shared nodes are assigned identical global node identifiers. Figure 2 provides a detailed illustration of an example of a two-by-two element grid (degree of freedom, DOF) for the 8-node configuration

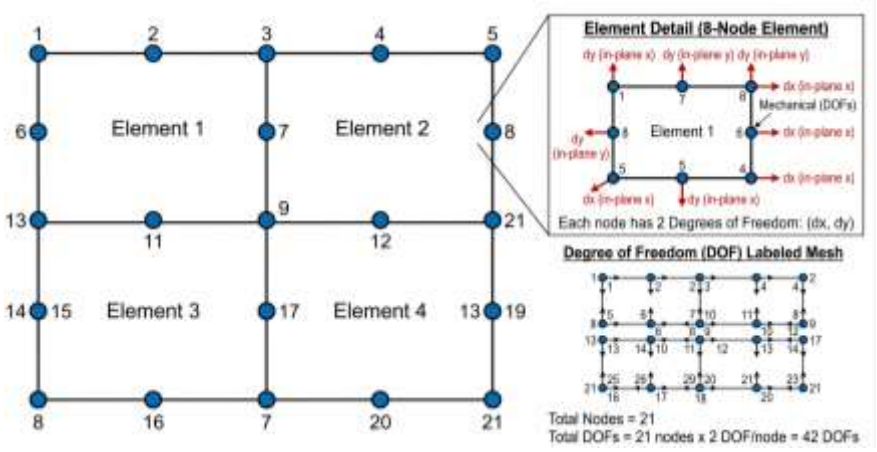


Figure 2. Natural Coordinates for 8 node Quadratic Quadrilateral Element

The element displacement field and strain vector are expressed as

$$\mathbf{u}^e(x,y) = \mathbf{N}_u(x,y)\mathbf{d}^e, \qquad \mathbf{S}^e = \mathbf{B}_u\mathbf{d}^e. \qquad (2)$$

The vector $\mathbf{d}^e$ contains the element displacement degrees of freedom, $\mathbf{N}_u$ is the displacement interpolation matrix, and $\mathbf{B}_u$ is the strain–displacement matrix. Derivatives with respect to physical coordinates are obtained through the isoparametric Jacobian. Element connectivity and positive Jacobian determinants are checked at all integration points before assembly.Electrical variables are defined independently of the mechanical interpolation. Each piezoelectric element initially has an electrical variable representing the voltage difference across its thickness. For a linear through-thickness potential distribution,

$$\phi(z) = \phi_b + \frac{z}{t_p}v^e, \qquad E_z = -\frac{v^e}{t_p}. \qquad (3)$$

The coordinate z is measured from the lower piezoelectric surface towards the upper surface, t_p is the piezoelectric thickness, and $v^e = \phi_t - \phi_b$. More generally,

$$\mathbf{E}^e = \mathbf{B}_\phi v^e. \qquad (4)$$

The operator $\mathbf{B}_\phi$ contains the electric-field direction and the factor $-1/t_p$. The polarization direction and orientation of the piezoelectric material axes determine the signs of the coupling coefficients. The linear piezoelectric response is expressed in stress-charge form as

$$\mathbf{T} = \mathbf{C}^E\mathbf{S} - \mathbf{e}^T\mathbf{E}, \qquad \mathbf{D} = \mathbf{e}\mathbf{S} + \boldsymbol{\varepsilon}^S\mathbf{E}. \qquad (5)$$

Here, $\mathbf{C}^E$, $\mathbf{e}$, and $\boldsymbol{\varepsilon}^S$ are the elastic stiffness, piezoelectric stress, and dielectric permittivity matrices, respectively. The element matrices are calculated as

$$\mathbf{k}^e_{uu} = \int_{\Omega_e} \mathbf{B}_u^T\,\mathbf{C}^E\mathbf{B}_u\,d\Omega, \qquad (6)$$

$$\mathbf{k}^e_{u\phi} = -\int_{\Omega_e^p} \mathbf{B}_u^T\,\mathbf{e}^T\mathbf{B}_\phi\,d\Omega, \quad \mathbf{k}^e_{\phi u} = \left(\mathbf{k}^e_{u\phi}\right)^T, \qquad (7)$$

$$\mathbf{k}^e_{\phi\phi} = \int_{\Omega_e^p} \mathbf{B}_\phi^T\,\boldsymbol{\varepsilon}^S\mathbf{B}_\phi\,d\Omega. \qquad (8)$$

The domain Ω_e^p denotes the piezoelectric region. The aluminium layer contributes to mechanical stiffness but has no piezoelectric coupling contribution. For the two-dimensional formulation, the integration measure includes the specified out-of-plane width or unit-width assumption. The element matrices are assembled using the global connectivity. Element electrical variables belonging to the same continuous electrode pair are constrained to a common voltage through an electrode transformation matrix. Consequently, each independently connected electrode pair has one voltage degree of freedom. After electrode condensation, the static system is

$$\begin{bmatrix} \mathbf{K}_{uu} & \mathbf{K}_{u\phi} \\ \mathbf{K}_{\phi u} & -\mathbf{K}_{\phi\phi} \end{bmatrix} \begin{bmatrix} \mathbf{U} \\ \mathbf{\Phi} \end{bmatrix} = \begin{bmatrix} \mathbf{F} \\ \mathbf{0} \end{bmatrix}. \qquad (9)$$

All displacement degrees of freedom at the clamped end are prescribed as zero. The remaining mechanical degrees of freedom are unconstrained except where the external load is applied. The lower electrode is grounded, and the upper electrode is equipotential with an unknown voltage. The zero electrical right-hand side represents zero prescribed net free charge on each isolated electrode under an initially uncharged open-circuit condition; it does not require the local electric displacement to vanish.

After eliminating prescribed degrees of freedom, Equation (9) is solved for displacement and electrode voltage. Mesh convergence is assessed using the unsmoothed tip displacement and electrode voltage. The mesh sequence, response values, convergence tolerance, and final mesh are reported to establish the numerical resolution of the solution. Where moving-average smoothing is used for visualization, it is applied only after solving the finite element equations:

$$\bar{x}_i = \frac{1}{|\mathcal{W}_i|} \sum_{j \in \mathcal{W}_i} x_j \,. \qquad (11)$$

The set $\mathcal{W}_i$ contains spatially ordered samples within the averaging window, and $|\mathcal{W}_i|$ is the number of included samples. The sampling path, window size, and endpoint treatment must be specified. Averaging by arbitrary global node number is avoided because consecutive identifiers need not represent neighbouring locations.

3. Parametric Study of PCB Beams

A controlled parametric study was conducted to evaluate the effects of beam length, beam width, and applied force on displacement and voltage output. Each parameter was varied independently while the remaining dimensions and loading conditions were held constant. For the length study, beam and piezoelectric layer lengths of 80, 100, 120, and 140 mm were analysed at a fixed width of 40 mm and thickness of 1 mm . For the width study, beam and piezoelectric layer widths of 40, 60, and 80 mm were analysed at a fixed length of 120 mm and thickness of 1 mm. A force of 1.2 N was applied at the free end in both geometric studies. For the force study, the beam dimensions were fixed at 140 mm × 40 mm × 1 mm (length × width × thickness), and the applied force was varied from 0.05 to 1.2 N. Each force was applied at the free end, and the resulting displacement and voltage output were evaluated. All configurations used the same mechanical and electrical boundary conditions. A clamped-free mechanical condition was imposed by constraining displacement at the clamped end and leaving the opposite end unconstrained except for the applied load. Equipotential conditions were imposed on the modelled electrodes. The same response-extraction procedure was used across all configurations to enable consistent comparisons. Results obtained using the developed eight-node quadrilateral element were compared with previously published results to assess agreement with the reference model.

4. Result and discussion

The eight-node finite element model incorporating moving-average processing (FEM-MA) was evaluated by comparing its predicted displacement and electrical potential with those obtained from the conventional FEM model and ANSYS. The MATLAB models were solved under static loading, whereas the ANSYS model was evaluated using harmonic response analysis at 0.1 Hz to approximate quasi-static conditions. This comparison assumes that the excitation frequency is sufficiently below the relevant natural frequencies and that inertial and damping effects are negligible.

Table 2. Comparison of displacement and electrical potential predicted by FEM-MA, conventional FEM, and ANSYS at 30,000 elements.

Model	Displacement (mm)	Electrical potential (mV)
FEM-MA	1.2161×10^{-8}	1.1376
Conventional FEM	2.4348×10^{-8}	0.4848
ANSYS	1.2619×10^{-8}	1.1226

As shown in Table 2, the FEM-MA predictions are closer to the ANSYS results than those of the conventional FEM model. Taking ANSYS as the reference, the FEM-MA displacement differs by approximately 3.6%, and its electrical potential differs by approximately 1.3%. The conventional FEM model overpredicts displacement by approximately 92.9% and underpredicts electrical potential by approximately 56.8%. These results indicate improved agreement between FEM-MA and ANSYS for the configuration examined. Figure 3 compares the electrical potential predicted with and without moving-average processing as the number of elements increases. Both predictions increase with mesh refinement, while FEM-MA produces consistently higher electrical potentials. At the finest mesh shown, the reported values are approximately 1.14 with MA and 0.49 without MA, expressed in the same voltage unit.

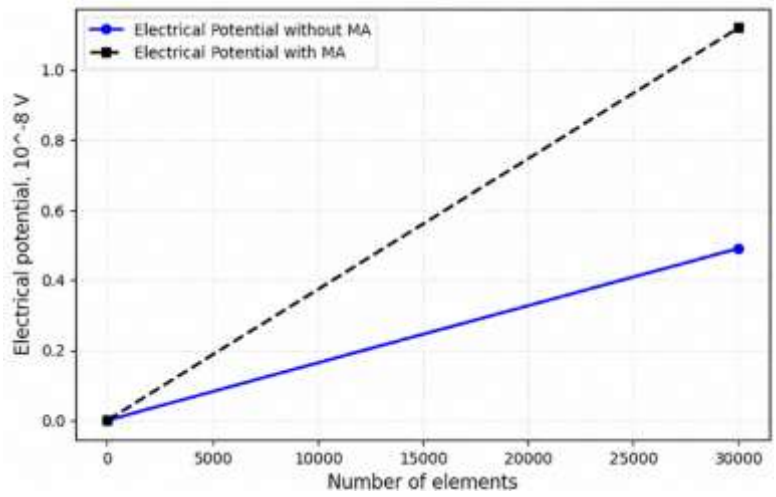


Figure 3. Effect of mesh refinement on electrical potential predicted with and without moving-average processing.

This difference demonstrates that the predicted electrical potential is sensitive to the processing method.The closer agreement with ANSYS supports the FEM-MA prediction for the case examined. However, smoothing alone does not establish numerical accuracy or mesh convergence. Convergence should be assessed from the change in the predicted response between successive mesh refinements, and the effect of window size should be evaluated separately. The influence of moving-average window size on the displacement distribution is illustrated in Figure 4 for a mesh containing 4,800 elements. Windows of 100 and 400 samples were compared to examine the sensitivity of the processed response to the averaging interval. A larger window generally produces stronger smoothing but may also suppress local variations. Window selection should therefore consider both the reduction of numerical fluctuations and the preservation of the underlying displacement distribution.

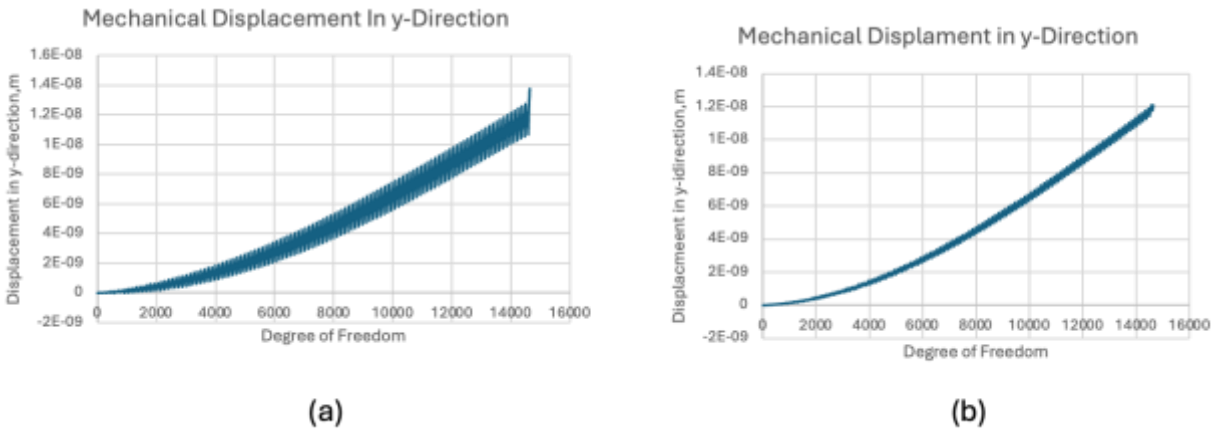


Figure 4. Noisy results of Displacement distributions when the window size is (a) 100 and (b) 400

The influence of beam width was investigated while maintaining a beam length of 120 mm and a thickness of 1 mm under an applied force of 1.2 N . Table 3 summaries the predicted displacement and electrical potential for widths of 40, 60, and 80 mm.

Table 3 Effect of beam width on displacement and electrical potential

Width, mm	Displacement (mm)	Electrical Potential (mV)
40	3.1790×10^{-7}	29.85
60	1.0854×10^{-7}	10.20
80	5.3811×10^{-8}	5.06

Both displacement and electrical potential decrease as beam width increases. The 40 mm beam produces the largest displacement, 3.1790×10^{-7} mm, and the highest electrical potential, 29.85 mV. Increasing the width to 80 mm reduces these values to 5.3811×10^{-8} mm and 5.06 mV, respectively. These changes correspond to reductions of approximately 83% in both responses. The trend is consistent with the greater bending stiffness of a wider beam under the same applied force. Increased stiffness limits deformation and reduces the strain available to generate an electrical response in the piezoelectric layer. Within the investigated width range, the 40 mm beam therefore provides the highest predicted voltage. Figure 5 presents the corresponding responses for the three beam widths.

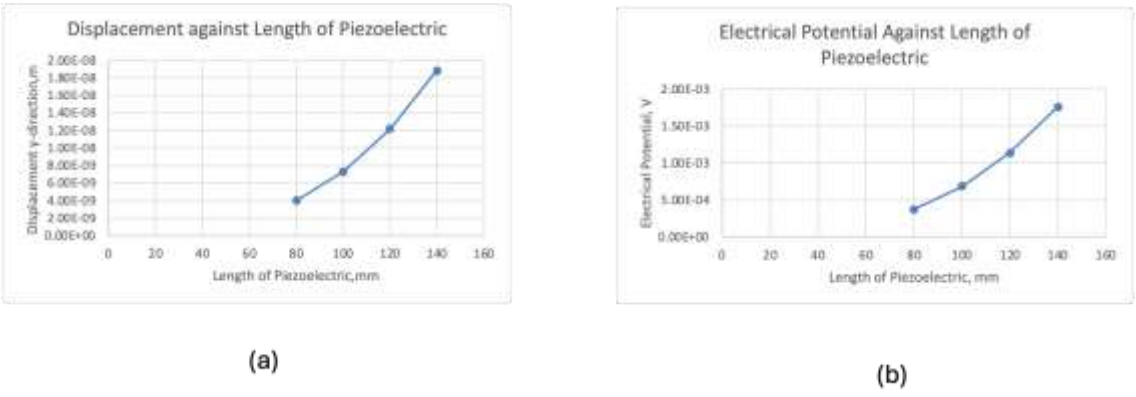


Figure 5. (a) simulated displacement responses of piezoelectric beams with various lengths of piezoelectric (b) simulated electrical responses of piezoelectric beams with various lengths of piezoelectric

The influence of beam length was investigated for beams with a fixed width of 40 mm and thickness of 1 mm under an applied force of 1.2 N. Table 4 presents the results for lengths ranging from 80 to 140 mm.

Table 4. Effect of beam length on displacement and electrical potential under an applied force of 1.2 N.

Length (mm)	Displacement (mm)	Electrical Potential (mV)
80	1.0854×10^{-7}	10.19
100	1.9414×10^{-7}	18.22
120	3.1790×10^{-7}	29.83
140	4.8709×10^{-7}	45.69

Displacement and electrical potential increase with beam length. The 80 mm beam produces a displacement of 1.0854 × 10^{-7} mm and an electrical potential of 10.19 mV. At 140 mm, these values increase to 4.8709 × 10^{-7} mm and 45.69 mV, respectively. Thus, increasing the length from 80 to 140 mm increases both responses by approximately 4.5 times. For a cantilever subjected to the same transverse tip force, increasing the length increases the bending moment near the fixed support and reduces the effective bending stiffness. The resulting changes in deformation and strain are consistent with the higher electrical potential predicted for the longer beams. Figure 6 shows the corresponding responses for each beam length. Among the lengths investigated, the 140 mm beam provides the highest predicted voltage. Whether this length is suitable for a particular application depends on additional constraints, including available space and allowable deformation

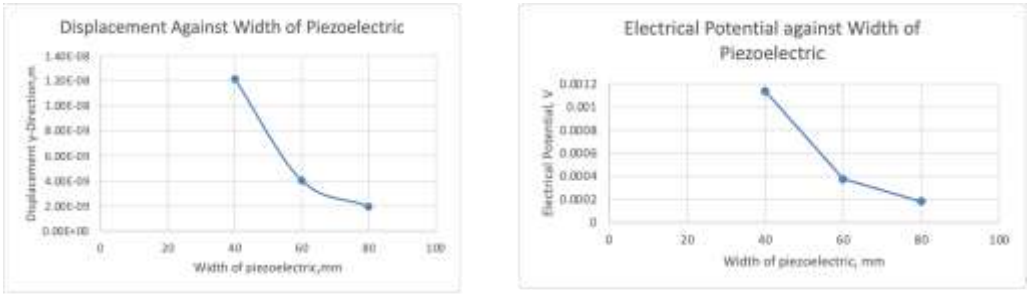


Figure 6. (a) simulated displacement responses of piezoelectric beams with various widths of piezoelectric (b) simulated electrical responses of piezoelectric beams with various widths of piezoelectric

A beam measuring 140 mm in length, 40 mm in width, and 1 mm in thickness was selected for further load-response analysis. Although the 140 mm beam produces a higher voltage in the length study, the available results do not establish a unique optimal geometry. The 120 mm configuration is therefore treated here as the selected design. Table 5 presents its displacement and electrical potential under applied forces ranging from 0.05 to 1.2 N

Table 5. Effect of applied force on displacement and electrical potential for the selected 120 × 40 × 1 mm beam

Force (N)	Displacement (mm)	Electrical Potential (mV)
0.05	1.3246×10^{-8}	1.24
0.1	2.6491×10^{-8}	2.49
0.15	3.9737×10^{-8}	3.73
0.2	5.2983×10^{-8}	4.97

1.2	3.1790×10^{-7}	29.83

Both responses increase approximately linearly with applied force, as illustrated in Figure 7. Increasing the force from 0.05 to 1.2 N, a factor of 24, increases displacement and electrical potential by approximately the same factor. At the highest force, the beam produces a displacement of 3.1790×10^{-7} mm and an electrical potential of 29.83 mV. This proportional response is consistent with the linear behaviour assumed in the model.

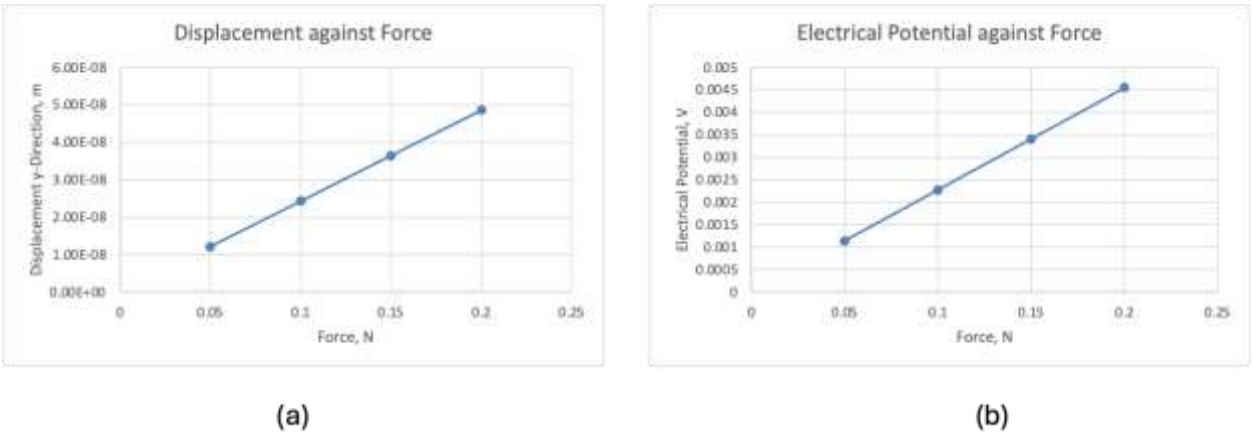


Figure 7. (a) simulated displacement responses of piezoelectric beams with various forces of piezoelectric (b) simulated electrical responses of piezoelectric beams with various forces of piezoelectric

The higher electrical potential results from the increased mechanical strain induced by the larger applied force. These findings describe the load sensitivity of the selected geometry and provide a basis for further investigation under application-specific loading. The present results quantify displacement and electrical potential under static or quasi-static conditions. Assessment of biomedical energy-harvesting performance additionally requires electrical power measurements or predictions under a defined circuit load and representative time-varying excitation. Voltage alone is insufficient to establish harvested power or suitability for a biomedical device.

5. Conclusion

The connection between the mechanical and electrical domains isestablished by the electromechanical equations controlling PZT energy harvesters, which makes it useful to predict displacement and electrical potential. These formulas, which are shown as a coupled matrix system in FEM, consist of stiffness matrix, mass matrix, piezoelectric coupling matrix, and dielectric matrix to determine the displacement and electrical potential from PZT beams. The MATLAB code for analysing electromechanical interactions in piezoelectric beams under linear static analysis has also been successfully developed. The finite element method (FEM) was employed tosolve electromechanical equations to determine displacement and electric potential by using quadratic quadrilateral elements. The FEM code also solves the electromechanical equations in piezoelectric beams to determine displacement and electrical potential. The piezoelectric effect is crucial to these simulations because it combines the beam's mechanical deformation with the creation of electrical potential. An electrical charge is induced on the surface of the piezoelectric material by mechanical stress-induced deformation, which results in the generation of an electrical potential. Both displacement and electrical potential in piezoelectric beams may be measured due to the FEM code's ability to accurately represent this electromechanical relationship. By successfully including the piezoelectric effect in the study, this method allows for a thorough comprehension of how piezoelectric energy harvesters behave. A parametric study was then conducted to examine the effects of beam length, width, and applied force on performance. The results show that the beam with a length of 140 mm, a width of 40 mm, and a thickness of 1 mm produced the highest displacement, leading to greater electrical potential, reaching 29.83 mV under a force of 1.2 N applied at the beam tip. The study also confirmed that

increasing beam length and applied force, while reducing beam width, leads to higher displacement and electrical potential. These findings provide useful guidance for improving the design and efficiency of piezoelectric beams for biomedical energy-harvesting applications.

Acknowledgement
The authors would like to acknowledge the Ministry of Higher Education Malaysia for the Fundamental Research Grant Scheme with Project Code: FRGS/1/2021/TK0/USM/03/3/.

Conflict of interest: The authors declare no conflict of interest regarding the publication of the paper.

AI Use Statement:
During the preparation of this manuscript, the authors used Grammarly software solely for language refinement. No AI tools were used for data analysis, interpretation, or generation of scientific content. All outputs were critically reviewed and edited by the authors. The authors take full responsibility for the integrity and accuracy of the work.

Reference

1. Zhou, W., Du, D., Cui, Q., Lu, C., Wang, Y., & He, Q. (2022). Recent Research Progress in Piezoelectric Vibration Energy Harvesting Technology. *Energies*, *15*(3). https://doi.org/10.3390/en15030947

2. J. Roy, M. Madni, A. Sau, R. Basu, and S. Das, "Advances and crosslinking of the piezoelectric nanoplatform: exploring the multifunctionality in different biomedical applications," *Front. Chem.*, vol. 13, Nov. 2025, https://doi: 10.3389/fchem.2025.1714203.

3. Anton, S. R., & Sodano, H. A. (2007). A review of power harvesting using piezoelectric materials (2003–2006). *Smart Materials and Structures*, 16(3), R1 R21. https://doi.org/10.1088/0964-1726/16/3/R01

4. Saida, M., Zaibi, G., Samet, M., & Kachouri, A. (2019). Design Optimisation of Piezoelectric Energy Harvesting Cantilevers for Medical Devices. *Journal of Communications Software and Systems*, *15*(4), 301–310. https://doi.org/10.24138/jcomss.v15i4.770

5. Hosseini, R., Hamedi, M., Im, J., Kim, J., & Dayou, J. (2017). Analytical and experimental investigation of partially covered piezoelectric cantilever energy harvester. *International Journal of Precision Engineering and Manufacturing*, *18*(3), 415–424. https://doi.org/10.1007/s12541-017-0050-3

6. Rosa, M., & De Marqui Junior, C. (2014). Modeling and analysis of a piezoelectric energy harvester with varying cross-sectional area. *Shock and Vibration*, *2014*. https://doi.org/10.1155/2014/930503

7. Mohamed, K., Elgamal, H., & Kouritem, S. A. (2021). An experimental validation of a new shape optimisation technique for piezoelectric harvesting cantilever beams. *Alexandria Engineering Journal*, *60*(1), 1751-1766. https://doi.org/10.1016/j.aej.2020.11.024

8. Kramer, B., & Qian, E. (2026). Reduced-order modeling for engineering systems: Survey and opportunities for digital twins. *Structural and Multidisciplinary Optimization, 69*, Article 141. https://doi.org/10.1007/s00158-026-04310-0

9. Wang, P., Zhao, Y., Guo, R. (2026) Power Flow Analysis of a Uniform Beam and an Acoustic Black Hole Beam Coupled with Springs Using the Isogeometric Approach. International Journal of Structural Stability and Dynamics. https://doi.org/10.1142/S0219455427504141

10. M. C. de Jong, K. C. Kosaraju, and J. M. A. Scherpen, "On control of voltage-actuated piezoelectric beam: A Krasovskii passivity-based approach," *Eur. J. Control*, vol. 69, p. 100724, Jan. 2023, doi: 10.1016/j.ejcon.2022.100724.

11. F. H. Syed, L. W. Thong, M. F. Baig, Y. K. Chan, and M. N. E. Efzan, "A Comparative Study of Material and Structural Configurations in Piezoelectric Energy Harvesting," *Emerging Science Journal*, vol. 9, no. 1, pp. 346–361, Feb. 2025, doi: 10.28991/ESJ-2025-09-01-019.

12. J. Dewanjee and M. S. Islam, "Piezoelectric based V-shape cantilever beam design of energy harvester for biomedical applications," *International Review of Applied Sciences and Engineering*, vol. 15, no. 1, pp. 73–81, Jan. 2024, doi: 10.1556/1848.2023.00652.

13. K. K. Das, B. Basu, P. Maiti, and A. K. Dubey, "Piezoelectric nanogenerators for self-powered wearable and implantable bioelectronic devices," *Acta Biomater.*, vol. 171, pp. 85–113, Nov. 2023, doi: 10.1016/j.actbio.2023.08.057.

14. P. Tripathi and A. K. Dubey, "Role of Piezoelectricity in Disease Diagnosis and Treatment: A Review," *ACS Biomater. Sci. Eng.*, vol. 10, no. 10, pp. 6061–6077, Oct. 2024, doi: 10.1021/acsbiomaterials.4c01346.

15. M. G. Abdelmageed, A. M. R. Fath El-Bab, A. A. Abouelsoud, and M. Elsisy, "Energy harvesting from pulsatile Superior Vena Cava for implantable devices," *Sens. Actuators A Phys.*, vol. 395, p. 116993, Dec. 2025, doi: 10.1016/j.sna.2025.116993.

16. K. K. Das, R. Pandey, and A. K. Dubey, "Piezo-electronics: A paradigm for self-powered bioelectronics," *Biomaterials*, vol. 318, p. 123118, Jul. 2025, doi: 10.1016/j.biomaterials.2025.123118.

17. M. Chahari, E. Salman, M. Stanacevic, R. Willing, and S. Towfighian, "Performance of piezoelectric and triboelectric transducers under gait loading for energy harvesting and load monitoring in total knee replacements," *Nano Energy*, vol. 141, p. 111117, Aug. 2025, doi: 10.1016/j.nanoen.2025.111117.

18. O. Abdalla *et al.*, "3D printed CNT/TPU triboelectric nanogenerator for load monitoring of total knee replacement," *Smart Mater. Struct.*, vol. 34, no. 6, p. 065030, Jun. 2025, doi: 10.1088/1361-665X/ade1ba.

19. M. Shekari, G. Naderi, S. Moghari, M. Naqvi, and H. A. Khonakdar, "Piezoelectric Materials for Energy Harvesting in Wearables," *Polym. Eng. Sci.*, vol. 65, no. 12, pp. 6451–6478, Dec. 2025, doi: 10.1002/pen.70186.

20. D. Singh *et al.*, "Piezoelectric Energy Harvesting for Pacemaker Applications: Current State-of-the-Art, Materials, Design, and Alternative Technologies," *ACS Biomater. Sci. Eng.*, vol. 11, no. 8, pp. 4570–4620, Aug. 2025, doi: 10.1021/acsbiomaterials.5c00298.

21. K. K. Das, B. Basu, P. Maiti, and A. K. Dubey, "Piezoelectric nanogenerators for self-powered wearable and implantable bioelectronic devices," *Acta Biomater.*, vol. 171, pp. 85–113, Nov. 2023, doi: 10.1016/j.actbio.2023.08.057.

22. S. Choudhury, Z. L. Wang, and S.-W. Kim, "Hydrogel-based piezoelectric materials and devices for implantable bioelectronics," *Biomaterials*, vol. 327, p. 123768, Apr. 2026, doi: 10.1016/j.biomaterials.2025.123768.

23. A. Sohail *et al.*, "Integrating self-powered medical devices with advanced energy harvesting: A review," *Energy Strategy Reviews*, vol. 52, p. 101328, Mar. 2024, doi: 10.1016/j.esr.2024.101328.

24. M. Hamza *et al.*, "Recent progress in 3D printed piezoelectric materials for biomedical applications," *Materials Science and Engineering: R: Reports*, vol. 164, p. 100962, Jun. 2025, doi: 10.1016/j.mser.2025.100962.

25. J. Roy, M. Madni, A. Sau, R. Basu, and S. Das, "Advances and crosslinking of the piezoelectric nanoplatform: exploring the multifunctionality in different biomedical applications," *Front. Chem.*, vol. 13, Nov. 2025, doi: 10.3389/fchem.2025.1714203.

26. N. Almarri, J. Chang, W. Song, D. Jiang, and A. Demosthenous, "Piezoelectric energy harvesting and ultra-low-power management circuits for medical devices," *Nano Energy*, vol. 131, p. 110196, Dec. 2024, doi: 10.1016/j.nanoen.2024.110196.

27. B. P. Yalagala, J. Zhang, R. Das, and H. Heidari, “Advancements in Energy Harvesting for Implantable Cardiovascular Devices,” 2025, pp. 25–54. doi: 10.1007/978-3-031-52834-7_2.
28. A. I. Sadaf, M. Mohiuddin, R. Ahmed, D. Meade, K. Akter, and H. Ahmed, “Harnessing vibrations: A review on structural architecture and design ideology of the cantilever beam based piezoelectric energy harvesters,” *Appl. Energy*, vol. 396, p. 126286, Oct. 2025, doi: 10.1016/j.apenergy.2025.126286.

29. A. Erturk and D. J. Inman, “A Distributed Parameter Electromechanical Model for Cantilevered Piezoelectric Energy Harvesters,” *J. Vib. Acoust.*, vol. 130, no. 4, Aug. 2008, doi: 10.1115/1.2890402.

30. P. Peralta-Braz, M. M. Alamdari, R. O. Ruiz, E. Atroshchenko, and M. Hassan, “Design optimisation of piezoelectric energy harvesters for bridge infrastructure,” *Mech. Syst. Signal Process.*, vol. 205, p. 110823, Dec. 2023, doi: 10.1016/j.ymssp.2023.110823.

31. D. Man *et al.*, “Enhanced energy harvesting from random excitations: A dynamic amplifier-augmented hybrid bistable piezoelectric energy harvester,” *Alexandria Engineering Journal*, vol. 103, pp. 21–29, Sep. 2024, doi: 10.1016/j.aej.2024.06.020.

32. D. Man *et al.*, “Improving energy harvesting from low-frequency excitations by a hybrid tri-stable piezoelectric energy harvester,” *Alexandria Engineering Journal*, vol. 76, pp. 153–165, Aug. 2023, doi: 10.1016/j.aej.2023.06.031.

33. M. Rosa and C. De Marqui Junior, “Modeling and Analysis of a Piezoelectric Energy Harvester with Varying Cross-Sectional Area,” *Shock and Vibration*, vol. 2014, pp. 1–9, 2014, doi: 10.1155/2014/930503.

34. Skėrys, P., Gaidys, R. (2026) Optimal Shape Design of Cantilever Structure Thickness for Vibration Strain Distribution Maximization. Applied Sciences (Switzerland). https://doi.org/10.3390/app16020765